

Research Article

A Constitutive Model of Sandy Gravel Soil under Large-Sized Loading/Unloading Triaxial Tests

Pengfei Zhang,¹ Han Liu,¹ Zhentu Feng,² Chaofeng Jia,² and Rui Zhou³ 

¹Hebei Research Institute of Construction and Geotechnical Investigation Co. Ltd., Shijiazhuang 050031, China

²Luoyang Rail Transit Group Co Ltd., Luoyang 471000, Henan, China

³School of Civil Engineering, Beijing Jiaotong University, Beijing 100044, China

Correspondence should be addressed to Rui Zhou; 18121179@bjtu.edu.cn

Received 23 April 2021; Accepted 2 June 2021; Published 14 June 2021

Academic Editor: Faming Huang

Copyright © 2021 Pengfei Zhang et al. This is an open access article distributed under the Creative Commons Attribution License, which permits unrestricted use, distribution, and reproduction in any medium, provided the original work is properly cited.

Based on large-scale triaxial tests of sandy gravel materials, the strength and deformation characteristics under loading/unloading conditions are analyzed. At the same time, the applicability of the hyperbolic constitutive model to sandy gravel is studied using experimental data. The results indicate that sandy gravel under low confining pressures (0.2 and 0.4 MPa) shows a weak softening trend; the higher the confining pressure, the more obvious the hardening tendency (0.6 and 0.8 MPa) and the greater the peak strength. During unloading tests, strain softening occurs, and the peak strength increases with increasing confining pressure. During loading tests, dilatancy appears when the confining pressure is low (0.2 MPa). With increasing confining pressure (0.4, 0.6, and 0.8 MPa), the dilatancy trend gradually weakens, and the cumulative volumetric strain increases, which reflects the relevance of the stress paths. Through research, it is found that the hyperbolic constitutive model has good applicability to sandy gravel soils, and the corresponding model parameters are obtained.

1. Introduction

With the rapid development of rail transit, shield tunnel construction has encountered many severe challenges in sandy gravel strata in China. For example, the first phase of the Luoyang Urban Rail Transit Line 2 project under construction uses the shield method to cross the sandy gravel stratum, which is particularly important for the ground settlement, seepage damage, and the stability of the excavation surface [1–3]. In addition to a large number of field tests, the mechanical characteristics and description of the stress-strain relationship of coarse-grained soil are hot topics [4, 5], which can provide necessary conditions for numerical calculations in practical engineering.

The mechanical properties of soils are determined by many factors, including externally applied stress, soil type, microstructure damage [6], density, matrix suction caused by surface tension passing through the air in unsaturated environments [7], and temperature [8–10]. To date, many constitutive models of saturated/unsaturated soil have been

proposed, but there are still many controversies regarding some basic problems [9, 11], such as the selection of state variables of stress and strain and the theoretical framework of hydraulic coupling processes [12, 13]. Alonso et al. [14] established a constitutive model of unsaturated soil materials by utilizing the double-stress variables of net stress and matrix suction. Many scholars [15, 16] have discussed the hydraulic coupling characteristics of saturated/unsaturated soil and even some basic thermo-hydromechanical coupling characteristics [17, 18]. These theoretical studies considered the influence of the volume water content on mechanical properties, such as irreversible compression during drying and changes in the water content during loading/unloading. Based on the principle of thermodynamics, some researchers [19–21] established the hydraulic coupling effects of three-phase unsaturated soil by analyzing the thermodynamic potential of the solid-liquid-gas phase and dissipated energy. Recently, Bai et al. [22] proposed a thermo-hydromechanical constitutive model for geomaterials in view of the concept of particle rearrangement during the thermodynamic process

of porous granular materials, which is contributed to understand the mechanical properties of the particle movement of sandy gravel soils from the microscopic point of view.

For subway tunnel projects in sandy gravel strata [23–25], when discussing settlement control and deformation characteristics, the constitutive relationship of sandy gravel is rarely mentioned, and the commonly used Mohr–Coulomb relationship is still utilized [26]. The actual sandy gravel is a kind of coarse-grained soil; however, it is not reasonable to use the Mohr–Coulomb relationship. Therefore, it is particularly important to study the deformation characteristics of shield tunneling in sandy gravel formations and to determine the appropriate constitutive model and parameters [27, 28]. It has important engineering significance in stratum settlement control and station foundation pit excavation [29].

In this paper, a large-sized laboratory triaxial shear test is carried out on sandy gravel soil taken from the Luoyang subway site, and then triaxial shear tests on sandy gravel under different confining pressures are carried out to determine the appropriate sandy gravel constitutive model as well as the model parameters accordingly. This work can help with engineering design and practice. The established constitutive model can well reflect the loading process and unloading process of sandy gravel soil, which is also used for the numerical calculation during the unloading process in the shield tunnel excavation process.

2. Experiments of Large Sandy Gravel Soil under a Complex Stress Path

2.1. Test Schemes. This paper selects sandy gravel soil samples from the first phase of the project of Luoyang Urban Rail Transit Line 2 to conduct a large-scale triaxial test. The purpose is to investigate two typical stress state change processes (namely, loading and unloading stress paths) and then determine the stress-strain relationship characteristics and volumetric strain-axial strain characteristics, as well as the seepage effect [30, 31] and damage mechanism of the soil layer [24, 32, 33].

Actually, the stress and deformation state changes of the surrounding stratum are very complicated during the shield tunnel excavation process [34, 35], even related to the effect of environmental temperature [36, 37] and the thermal-mechanical behavior of tunnel lining segments [38, 39]. For simplicity, this test simulates two extreme stress path change processes, namely, active failure and passive failure of the excavation surface. The specific test scheme is shown in Table 1, including 2 groups of tests. Among them, the sample size is 30 cm in diameter and 70 cm in height, and the test confining pressure is determined by the actual stress state at the site to be 200, 400, 600, and 800 kPa. The loading/unloading tests were accomplished by the stress-controlled method, and the shear rate was 0.2 kPa/s. This test primarily studies the strength and deformation characteristics of sandy gravel under triaxial compression and unloading conditions.

2.2. Preparation of Soil Samples. The soil layer in the project area is composed of silty clay, silt soil, a sand layer, and a gravel soil layer, which is a multilayer structure. According to the actual situation of the project, samples were taken at a depth of 10 m, and the dry density was controlled to be 2.27 g/cm^3 .

Through particle analysis, the maximum particle size of sandy gravel tested was 80 mm, and its characteristic particle size is shown in Table 2. The inhomogeneity coefficient of the soil is greater than 10, and the curvature coefficient is between 1 and 5. It belongs to coarse-grained soil with good gradation.

The test equipment was an SJ70 large-scale high-pressure triaxial shear tester. The test specimen has a diameter of 300 mm and a height of 700 mm. According to the sampling and sieving situation, the gravels that exceed the particle size limit of 60 mm account for only approximately 5%, so a particle size of 40–60 mm was used instead. The sample was prepared by splitting the soil into 5 layers. The sample preparation method uses a vibrator to vibrate. The static pressure of the vibrator bottom plate is 14 kPa, and the vibration frequency is 40 Hz. The vibration time is determined according to the dry density of the sample.

According to the actual engineering conditions and the high water permeability of sandy gravel, this test adopts the consolidated drained shear (i.e., CD) test. The sample saturation method adopts the suction saturation method.

3. Test Results and Analysis

3.1. Stress-Strain-Strength Characteristics. From the stress-strain relationship curves of sandy gravel in Figures 1 and 2, under the condition of the same shear rate, sandy gravel is loaded under low confining pressure (0.2 and 0.4 MPa), showing a weak softening trend. The higher the confining pressure, the more obvious the hardening tendency (0.6 and 0.8 MPa) and the greater the peak strength. For the unloading test, there is a more obvious softening phenomenon, and as the confining pressure increases, the peak value becomes more obvious. The deviator stress-strain curves of the two groups of sandy gravels show a strong nonlinear relationship when the stress and strain reach a certain value.

3.2. Volume Deformation Characteristics. Figures 3 and 4 give the $\varepsilon_v - \varepsilon_a$ relationship of sandy gravel when loading and unloading under different confining pressures. From Figure 3, under conditions of low confining pressure (0.2 MPa), sandy gravels exhibit shear shrinkage first and then dilatancy. As the confining pressure increases (0.4, 0.6, and 0.8 MPa), the dilatancy trend gradually weakens, and the cumulative body strain increases. Under unloading conditions (Figure 4), the main manifestation is dilatancy, and with increasing confining pressure, the dilatancy phenomenon becomes more obvious, which fully reflects the relevance of the stress path.

TABLE 1: Test schemes for large-size specimens.

Test number	Load path	Loading/unloading	Confining pressure (kPa)	Number of soil samples
1	$\sigma_3 = \text{constant}$, $\sigma_1 = \text{increases}$	Loading	200, 400, 600, 800	4
2	$\sigma_1 = \text{constant}$, $\sigma_3 = \text{decreases}$	Unloading	200, 400, 600, 800	4

TABLE 2: Particle gradation of sandy gravel samples.

Particle size (mm)	80	60	20	10	5	1	0.5	0.25	0.1
Cumulative percentage (%)	100	96.9	58.9	42.9	34.5	30.5	29.1	16.85	0

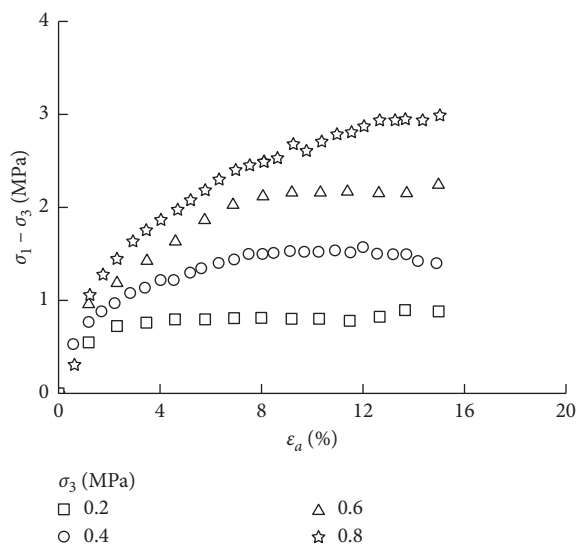


FIGURE 1: Axial stress-strain curve of sandy gravel soil under loading conditions.

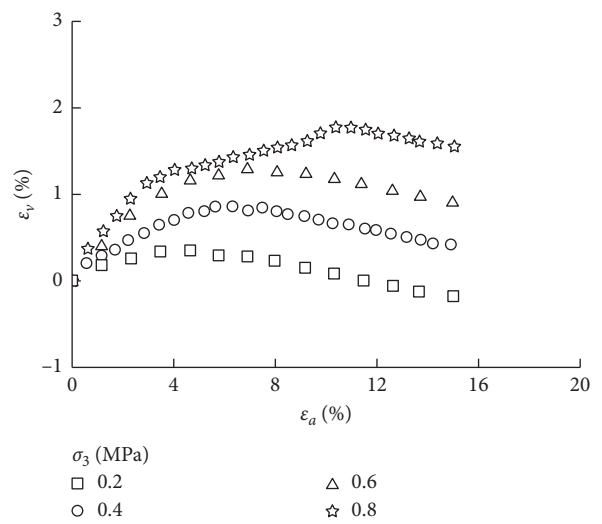


FIGURE 3: Curve of volumetric strain-axial strain under loading conditions.

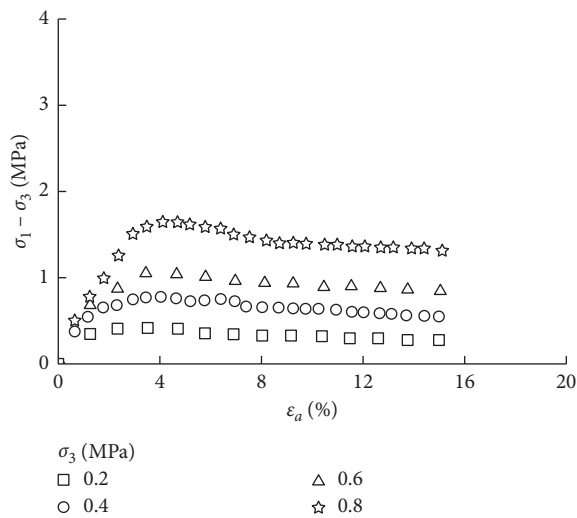


FIGURE 2: Axial stress-strain curve of sandy gravel soil under unloading conditions.

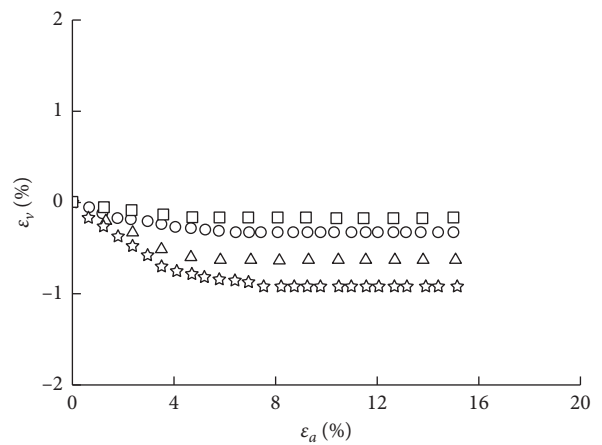


FIGURE 4: Curve of volumetric strain-axial strain under unloading conditions.

4. Constitutive Model of Sandy Gravel Considering the Loading/Unloading Process

Kondner [40] thought that the hyperbola can be used to fit the general triaxial test $(\sigma_1 - \sigma_3) - \varepsilon_1$ curve, namely,

$$(\sigma_1 - \sigma_3) = \frac{\varepsilon_a}{a + b\varepsilon_a}, \quad (1)$$

where a and b are test constants.

For the conventional triaxial shear test, $\varepsilon_a = \varepsilon_1$. Later, Duncan and Chang [41] proposed a widely used nonlinear elastic model, namely, the Duncan–Chang model, which was developed widely [42].

4.1. Conventional Triaxial Loading Test. Under conventional triaxial loading conditions, (1) can be written as

$$\frac{\varepsilon_1}{(\sigma_1 - \sigma_3)} = a + b\varepsilon_1, \quad (2)$$

where a is the intercept of the line and b is the slope of the line.

Obviously, there is an approximately linear relationship between $\varepsilon_1/(\sigma_1 - \sigma_3)$ and ε_1 . In the conventional triaxial shear test, the tangent elastic modulus can be expressed as

$$\begin{aligned} E_t &= \frac{d(\sigma_1 - \sigma_3)}{d\varepsilon_1}, \\ &= \frac{a}{(a + b\varepsilon_1)}. \end{aligned} \quad (3)$$

When $\varepsilon_1 = 0$ and $E_t = E_i$, the combination of (3) leads to

$$E_i = \frac{1}{a}. \quad (4)$$

When $\varepsilon_1 \rightarrow \infty$, from (1), we can get

$$(\sigma_1 - \sigma_3)_{\text{ult}} = \frac{1}{b}. \quad (5)$$

In (4) and (5), a represents the reciprocal of the initial elastic modulus E_i , and b represents the reciprocal of the ultimate deviator stress $(\sigma_1 - \sigma_3)_{\text{ult}}$ corresponding to the asymptote of the hyperbola.

In the conventional triaxial test, the shear strength $(\sigma_1 - \sigma_3)_f$ is determined according to the stress value corresponding to the strain value $\varepsilon_1 = 15\%$; for the stress-strain curve with a peak value, it generally takes its strength, that is, $(\sigma_1 - \sigma_3)_f = (\sigma_1 - \sigma_3)_{\text{peak}}$.

In this way, the damage ratio R_f can be defined as

$$R_f = \frac{(\sigma_1 - \sigma_3)_f}{(\sigma_1 - \sigma_3)_{\text{ult}}}. \quad (6)$$

Considering (5), one has

$$\begin{aligned} b &= \frac{1}{(\sigma_1 - \sigma_3)_{\text{ult}}}, \\ &= \frac{R_f}{(\sigma_1 - \sigma_3)_f}. \end{aligned} \quad (7)$$

Consider E_t as a function of stress, which can be obtained by transforming (2):

$$\varepsilon_1 = \frac{a(\sigma_1 - \sigma_3)}{1 - b(\sigma_1 - \sigma_3)}. \quad (8)$$

Substituting (8) into (3), we get

$$E_t = \frac{1}{a[1/(1 - b(\sigma_1 - \sigma_3))]^2}. \quad (9)$$

Substituting (4) and (7) into (9), we can get

$$E_t = E_i \left[1 - R_f \frac{(\sigma_1 - \sigma_3)}{(\sigma_1 - \sigma_3)_f} \right]^2. \quad (10)$$

According to the Mohr–Coulomb strength criterion, there is

$$(\sigma_1 - \sigma_3)_f = \frac{2c \cos \varphi + 2\sigma_3 \sin \varphi}{1 - \sin \varphi}. \quad (11)$$

The expression of the initial elastic modulus E_i with consolidation pressure σ_3 can be described as

$$E_i = K p_a \left(\frac{\sigma_3}{p_a} \right)^n, \quad (12)$$

where p_a is the atmospheric pressure ($p_a = 101.4$ kPa) and K and n are experimental parameters, representing the intercept and slope of the straight line between $\log(E_i/p_a)$ and $\log(\sigma_3/p_a)$.

Substituting (11) and (12) into (10), we can obtain

$$E_t = K p_a \left(\frac{\sigma_3}{p_a} \right)^n \left[1 - R_f \frac{(\sigma_1 - \sigma_3)(1 - \sin \varphi)}{2c \cos \varphi + 2\sigma_3 \sin \varphi} \right]^2. \quad (13)$$

In (13), the tangent elastic modulus E_t contains five material parameters (K , n , c , φ , and R_f). There is a hyperbolic relationship between the axial strain ε_1 and the confining strain $-\varepsilon_3$ based on the conventional triaxial loading test data of the soil (Figure 5).

The hyperbolic equation shown in Figure 5(a) can be written as

$$\varepsilon_1 = \frac{-\varepsilon_3}{f + D(-\varepsilon_3)}. \quad (14)$$

The linear equation in Figure 5(b) can be written as

$$\begin{aligned} -\left(\frac{\varepsilon_3}{\varepsilon_1} \right) &= f + D(-\varepsilon_3) \\ &= f - D(\varepsilon_3). \end{aligned} \quad (15)$$

When $\varepsilon_3 = 0$, $-\varepsilon_3/\varepsilon_1 = f = \nu_i$ is initial Poisson's ratio; when $-\varepsilon_3 \rightarrow \infty$, $D = 1/(\varepsilon_1)_{\text{ult}}$. The triaxial shear test shows that

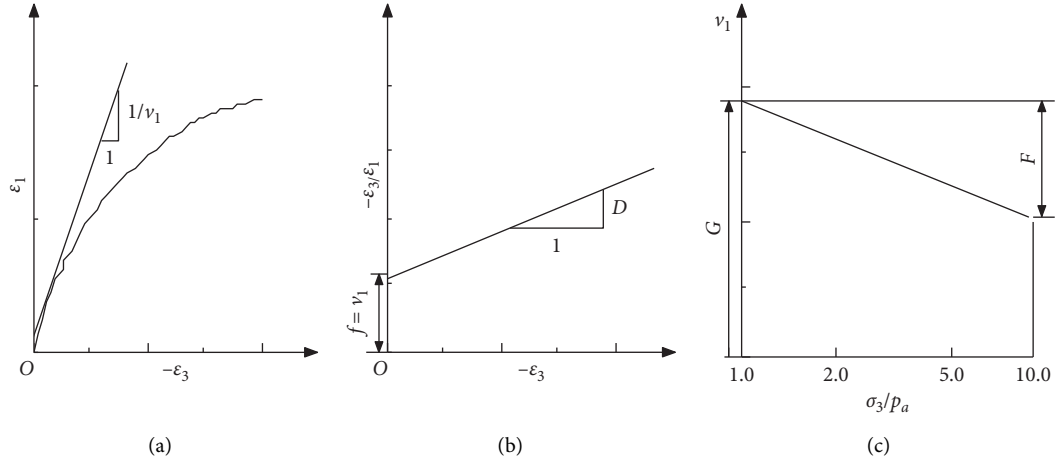


FIGURE 5: Determination of the relevant parameters of tangent Poisson's ratio: (a) ε_1 and $-\varepsilon_3$, (b) $-\varepsilon_3/\varepsilon_1$ and $-\varepsilon_3$, and (c) ν and $\log(\sigma_3/p_a)$.

initial Poisson's ratio is related to the confining pressure [9, 12]. As shown in Figure 5(c), it is assumed that

$$\begin{aligned} \nu_i &= f, \\ &= G - F \lg\left(\frac{\sigma_3}{p_a}\right), \end{aligned} \quad (16)$$

where G and F are test constants.

The difference of (14) induces

$$\begin{aligned} \nu_t &= \frac{-d\varepsilon_3}{d\varepsilon_1}, \\ &= \frac{\nu_i}{(1 - D\varepsilon_1)^2}. \end{aligned} \quad (17)$$

Substituting (8) and (16) into (17), we get

$$\nu_t = \frac{G - F \lg(\sigma_3/p_a)}{\left\{1 - D(\sigma_1 - \sigma_3)/(Kp_a(\sigma_3/p_a)^n [1 - R_f((\sigma_1 - \sigma_3)(1 - \sin \varphi))/(2c \cos \varphi + 2\sigma_3 \sin \varphi)]\right\}^2}. \quad (18)$$

4.2. Conventional Triaxial Unloading Test. Assuming that the soil is an isotropic medium, according to the generalized Hooke's law, the stress-strain relationship can be written as

$$E_t = \frac{\Delta\sigma_a(\Delta\sigma_a + \Delta\sigma_r) - 2\Delta\sigma_r^2}{\Delta\varepsilon_a(\Delta\sigma_a + \Delta\sigma_r) - 2\Delta\varepsilon_r\sigma_r}, \quad (19)$$

where $\Delta\sigma_a = \Delta\sigma_1$ is the axial stress increment, $\Delta\sigma_r = \Delta\sigma_3$ is the lateral stress increment, $\Delta\varepsilon_a = \Delta\varepsilon_1$ is the axial strain increment, and $\Delta\varepsilon_r = \Delta\varepsilon_3$ is the lateral strain increment.

When $\Delta\sigma_a = 0$ and $\Delta\sigma_r \neq 0$, the tangent elastic modulus E_t can be written as

$$\begin{aligned} E_t &= \frac{12\Delta\sigma_r}{\Delta\varepsilon_a - 2\Delta\varepsilon_r}, \\ &= \frac{\partial[2(\sigma_a - \sigma_r)]}{\partial(\varepsilon_a - 2\varepsilon_r)}. \end{aligned} \quad (20)$$

Referring to the derivation process of the triaxial loading test, under the condition of lateral unloading, the

relationship curve of $2(\sigma_{rc} - \sigma_r) - (\varepsilon_a - 2\varepsilon_r)$ is still satisfied with a hyperbolic relationship, namely, $(\varepsilon_a - 2\varepsilon_r)/2(\sigma_{rc} - \sigma_r) - (\varepsilon_a - \varepsilon_r)$.

Use (12) to establish the relationship between the initial tangent elastic modulus E_i and the axial consolidation pressure σ_{ac} . Here, E_i is actually the slope of the curve between $2(\sigma_{rc} - \sigma_r)$ and $(\varepsilon_a - 2\varepsilon_r)$ at the origin of the curve. Hence,

$$E_i = Kp_a \left(\frac{\sigma_{ac}}{p_a}\right)^n. \quad (21)$$

During lateral unloading, the failure deviator stress can be deduced:

$$(\sigma_a - \sigma_r)_f = \frac{2c \cos \varphi + 2\sigma_{ac} \sin \varphi}{1 + \sin \varphi}. \quad (22)$$

Because $\sigma_a = \sigma_{ac}$ is a constant during lateral unloading, it can be obtained from (20):

$$E_t = K p_a \left(\frac{\sigma_{ac}}{p_a} \right)^n \left\{ 1 - R_f \frac{(\sigma_{rc} - \sigma_r)(1 + \sin \varphi)}{2c \cos \varphi + 2\sigma_{ac} \sin \varphi - (\sigma_{ac} - \sigma_{rc})(1 + \sin \varphi)} \right\}. \quad (23)$$

The tangential elastic modulus E_t of the triaxial unloading test still contains 5 material constants (i.e., K , n , c , φ , and R_f). Comparing the unloading and loading paths, it can be seen that the axial strain ε_1 increases and ε_3 decreases. That is, the two effects on the test results are the same. From

this point of view, the calculation formula of Poisson's ratio for loading and unloading tests is the same. Therefore, the final expression of tangent Poisson's ratio in the unloading test is

$$v_t = \frac{G - F \lg(\sigma_3/p_a)}{\left\{ 1 - D(\sigma_1 - \sigma_3) / \left[K p_a (\sigma_3/p_a)^n \left[1 - r_f ((\sigma_1 - \sigma_3)(1 - \sin \varphi)) / (2c \cos \varphi + 2\sigma_3 \sin \varphi) \right] \right] \right\}^2}. \quad (24)$$

5. Determination of Loading/Unloading Parameters

5.1. Parameters of the Triaxial Loading. According to the stress-strain relationship shown in Figure 2, three groups of confining pressures and corresponding failure stresses $(\sigma_1 - \sigma_3)_f$ are obtained, as shown in Table 3. Thus, we can obtain the cohesive force $c = 19.2$ kPa and the friction angle $\varphi = 40^\circ$. In the coordinates of ε_1 and $\varepsilon_1/(\sigma_1 - \sigma_3)$, the relationship between the two is approximately linear (Figure 6). In Figure 6, a and b are the intercept and slope obtained by fitting a straight line. Combining equation (24), the E_i value can be obtained as shown in Table 4.

Figure 6 indicates that ε_1 and $\varepsilon_1/(\sigma_1 - \sigma_3)$ of sandy gravel have a good linear relationship, which means a hyperbolic relationship between shear stress and strain. The determination parameter R^2 values are all greater than 0.98, and the hyperbolic model has better applicability. Combining (7) can calculate the values of R_f to be 0.91, 0.93, and 0.92, and the average value is 0.92.

According to (12), the following expression can be obtained:

$$\lg\left(\frac{E_i}{p_a}\right) = \lg k + n \lg\left(\frac{\sigma_3}{p_a}\right). \quad (25)$$

From the results in Table 4, three sets of E_i and σ_3 values can be obtained. According to the fitting results, we can obtain the intercept $K=97$ and the slope $n=0.538$. According to the relationship between the axial strain of sandy gravel and the volume tric strain, the relationship of $-\varepsilon_3/\varepsilon_1$ and $-\varepsilon_3$ can be obtained as shown in Figure 7. Figure 7 indicates that there is a good linear relationship between $-\varepsilon_3/\varepsilon_1$ and $-\varepsilon_3$. By fitting the result to a straight line, the average value of the slope D is 0.07.

According to the three groups of values of v_i and σ_3 in Figure 7, the relationship between v_i and $\log(\sigma_3/p_a)$ is shown in Figure 8. Due to $v_i = G - F \lg(\sigma_3/p_a)$, the parameters $G=0.49$ and $F=0.186$ can be obtained.

5.2. Parameters for Triaxial Unloading. A large number of experimental studies [13–15] show that the cohesion c and

the friction angle φ in the unloading test are equal to those in the load test, that is, the cohesion c is 19.2 kPa and the friction angle φ is 40° . The damage ratio R_f of the unloading test is consistent with (26). In the coordinates $(\varepsilon_1 - 2\varepsilon_3)/2(\sigma_1 - \sigma_3) - (\varepsilon_1 - 2\varepsilon_3)$ (Figure 9), the linear fitting results are poor. This is because high or low stress levels will cause the test point to deviate from the straight line.

The relevant values obtained according to this method are shown in Table 5, and the fitted straight line relationship is shown in Figure 10. Combining the stress paths of the unloading test, there are

$$E_i = \frac{1}{a}, \quad (26)$$

$$2(\sigma_1 - \sigma_3)_{\text{ult}} = \frac{1}{b}, \quad (27)$$

where a and b are the intercepts and slopes obtained by fitting in Figure 4.

Combining the results in Figure 4, the relevant parameters of the unloading test and E_i and R_f can be obtained (Table 6). Finally, the average value of R_f in the sandy gravel unloading test can be obtained from Table 6, namely, $R_f=0.43$. Using (21), the following equation can be obtained:

$$\lg\left(\frac{E_i}{p_a}\right) = \lg K + \lg\left(\frac{\sigma_1}{p_a}\right), \quad (28)$$

where K represents the intercept and n represents the slope.

According to Table 6, three groups of E_i and σ_1 values can be obtained to fit a straight line, and the expression is

$$\lg\left(\frac{E_i}{p_a}\right) = 1 \cdot 6322 + 0 \cdot 759 \lg\left(\frac{\sigma_1}{p_a}\right). \quad (29)$$

Comparing (28) and (29), we can obtain that intercept $K=43$ and slope $n=0.759$. Finally, the parameters G , F , and D related to tangent Poisson's ratio are determined. Figure 5 shows the relationship between the axial strain and the body strain and the relationship between $-\varepsilon_3/\varepsilon_1$ and $-\varepsilon_3$ (Figure 11).

TABLE 3: Failure stress under loading conditions.

σ_3 (kPa)	$(\sigma_1 - \sigma_3)_f$ (kPa)	$(\sigma_1)_f$ (kPa)
200	800	1000
400	1529	1929
600	2238	2838

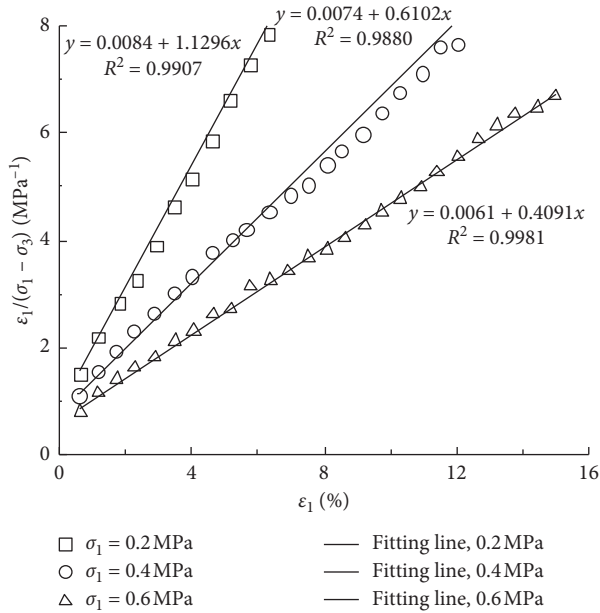


FIGURE 6: Relationship between ε_1 and $\varepsilon_1/(\sigma_1 - \sigma_3)$.

TABLE 4: Model parameters of the triaxial loading test (unit: MPa).

σ_3	a	b	E_i
0.2	0.0084	1.1296	119.05
0.4	0.0074	0.6102	135.14
0.6	0.0061	0.4091	163.93

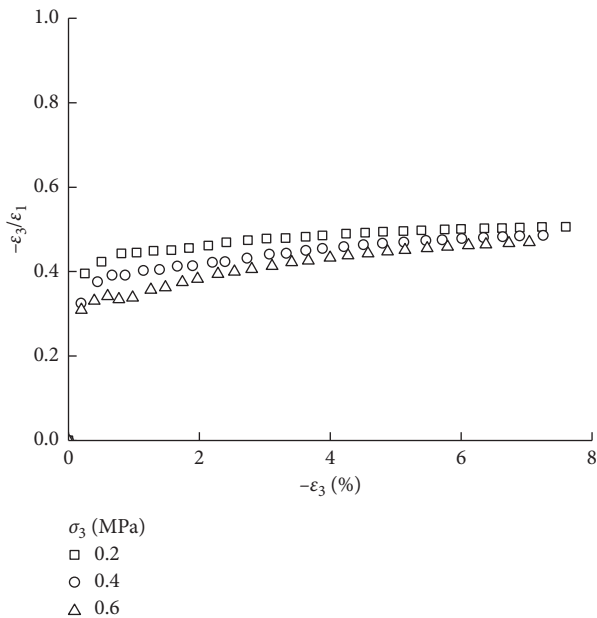


FIGURE 7: Relationship between $-\varepsilon_3/\varepsilon_1$ and $-\varepsilon_3$.

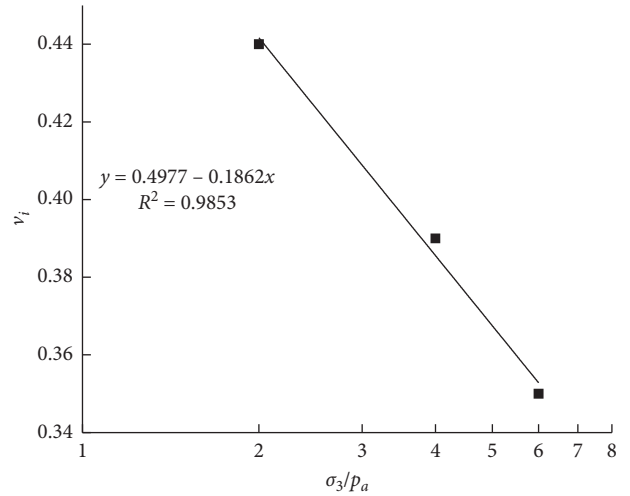


FIGURE 8: Relationship between ν_i and $\log(\sigma_3/Pa)$.

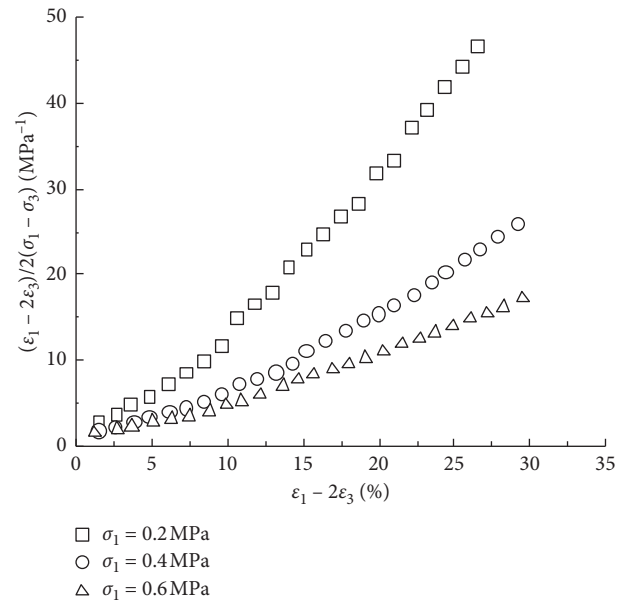


FIGURE 9: Relationship between $(\varepsilon_1 - 2\varepsilon_3)/2(\sigma_1 - \sigma_3)$ and $(\varepsilon_1 - 2\varepsilon_3)$.

TABLE 5: Failure stress under unloading conditions.

ε_1	$\varepsilon_1 - \varepsilon_3$		$\varepsilon_1 - 2\varepsilon_3$		$(\varepsilon_1 - 2\varepsilon_3)/2(\varepsilon_1 - \varepsilon_3)$	
	70%	90%	70%	90%	70%	90%
0.2	0.29	0.37	1.9	3.8	3.3	5.2
0.4	0.55	0.7	2.48	5.2	2.2	3.7
0.6	0.75	0.97	3.4	6.2	2.0	3.14

Figure 11 indicates that there is an obvious linear relationship between $-\varepsilon_3/\varepsilon_1$ and $-\varepsilon_3$, indicating that the assumption that the axial strain ε_1 and the lateral strain ε_3 are hyperbolic in the unloading test is applicable. The average value of the slope D of the fitted straight line is -0.015 . According to Figure 11, three groups of values of ν_i and σ_3

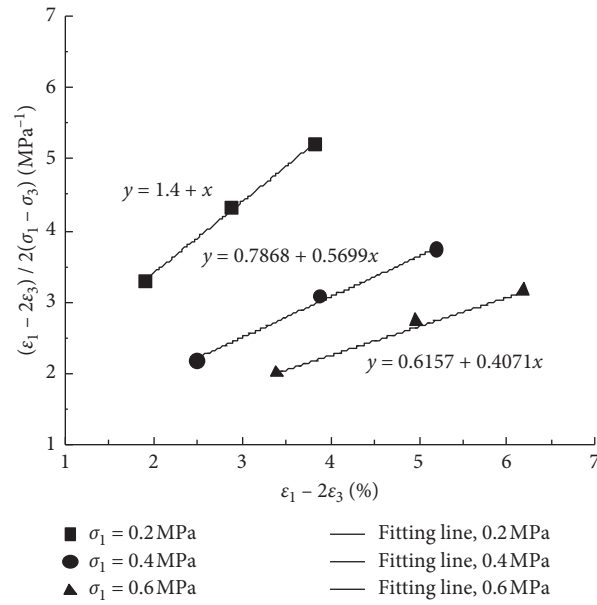


FIGURE 10: Relationship between $(\epsilon_1 - 2\epsilon_3)/2(\sigma_1 - \sigma_3)$ and $(\epsilon_1 - 2\epsilon_3)$.

TABLE 6: Model parameters of the triaxial unloading test (unit: MPa).

σ_1	a	b	E_i	R_f
0.2	0.014	1	71.43	0.42
0.4	0.0078	0.56	128.21	0.43
0.6	0.0062	0.41	162.60	0.43

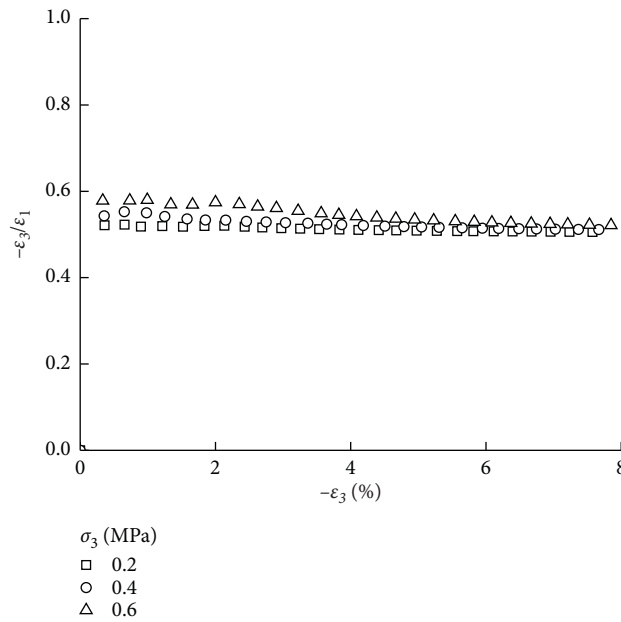
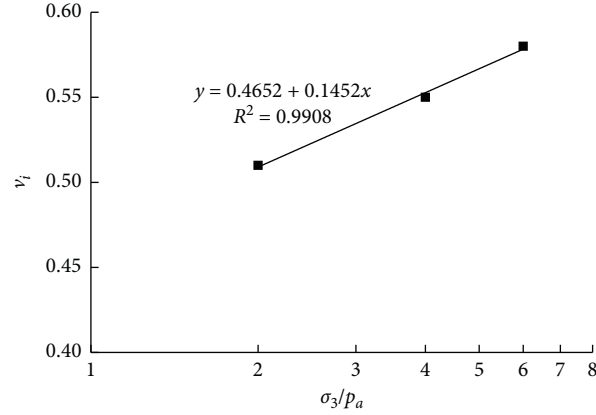


FIGURE 11: Relationship between $-\epsilon_3/\epsilon_1$ and $-\epsilon_3$.

FIGURE 12: Relationship between v_t and $\log(\sigma_3/p_a)$.

can be obtained, and the corresponding relationship between v_t and $\log(\sigma_3/p_a)$ can be drawn, as shown in Figure 12.

Due to

$$v_t = G - F \lg\left(\frac{\sigma_3}{p_a}\right), \quad (30)$$

the equation of the fitted straight line in Figure 12 is

$$v_t = 0.47 + 0.145 \lg\left(\frac{\sigma_3}{p_a}\right). \quad (31)$$

Comparing (30) and (31), the value of G is 0.47, and the value of F is -0.145 .

5.3. The Tangent Elastic Modulus and Tangent Poisson's Ratio.

For triaxial loading, according to the relevant parameters determined above, the tangent elastic modulus E_t and tangent Poisson's ratio v_t of sandy gravel under triaxial loading can be obtained as

$$E_t = 97 p_a \left(\frac{\sigma_3}{p_a}\right)^{0.538} \left[1 - 0.92 \frac{(\sigma_1 - \sigma_3)(1 - \sin \varphi)}{38 \cdot 4 \cos 40^\circ + 2\sigma_3 \sin 40^\circ} \right], \quad (32)$$

$$v_t = \frac{0.49 - 0.186 \lg(\sigma_3/p_a)}{\left\{ 1 - (0.07(\sigma_1 - \sigma_3)/97 p_a (\sigma_3/p_a)^{0.538} [1 - 0.92((\sigma_1 - \sigma_3)(1 - \sin \varphi))/(38 \cdot 4 \cos 40^\circ + 2\sigma_3 \sin 40^\circ)]) \right\}^2}. \quad (33)$$

For triaxial unloading, E_t and v_t during the unloading test are

$$E_t = 43 p_a \left(\frac{\sigma_3}{p_a}\right)^{0.759} \left[1 - 0.43 \frac{(\sigma_1 - \sigma_3)(1 - \sin \varphi)}{38 \cdot 4 \cos 40^\circ + 2\sigma_3 \sin 40^\circ} \right]^2, \quad (34)$$

$$v_t = \frac{0.47 + 0.145 \lg(\sigma_3/p_a)}{\left\{ (-0.015(\sigma_1 - \sigma_3))/43 p_a (\sigma_3/p_a)^{0.759} [1 - 0.43((\sigma_1 - \sigma_3)(1 - \sin \varphi))/(38 \cdot 4 \cos 40^\circ + 2\sigma_3 \sin 40^\circ)] \right\}^2}. \quad (35)$$

6. Conclusions

Consolidation and drainage shear tests of sandy gravel under different confining pressures under loading/unloading conditions are carried out. The differences in the strength and deformation of sandy gravel are analyzed. In using the proposed model, the parameters are few and can be obtained

from normal geotechnical tests, which has high application value in practical engineering. The main conclusions drawn are as follows:

- (1) The relationships between $\sigma_1 - \sigma_3$ and ε_1 and ε_v and ε_a of sandy gravel soil under loading conditions are all nonlinear. The smaller the confining pressure, the

weaker the stress-strain relationship. The stress-strain relationship exhibits a softening phenomenon, and the bulk strain undergoes dilatancy deformation. In contrast, it shows strain hardening and shear shrinkage deformation.

- (2) Under unloading conditions, the sandy gravel soil softens significantly with increasing confining pressure, and the peak strength increases. In the meantime, the tric strain response exhibits dilatancy characteristics. The strength and deformation characteristics of sandy gravel soil have a high dependence on the stress path.
- (3) The Duncan–Chang hyperbolic model has good applicability for simulating sandy gravel soils, and the model parameters are calculated according to the test results, which can provide help for engineering design and practice.

Abbreviations

$\varepsilon_1, \varepsilon_3$:	Principal strains
ε_r :	Lateral strain
ε_v :	Bulk strain
σ_1, σ_3 :	Principal stresses
σ_{rc} :	Lateral consolidation pressure
σ_r :	Lateral pressure
E_t :	Tangent elastic modulus
E_i :	Initial modulus of elasticity
c :	Cohesion
φ :	Internal friction angle
p_a :	Atmospheric pressure
K, n, G, F :	Material test constants
ν_i :	Initial Poisson's ratio.

Data Availability

The data used to support the findings of this study are available from the corresponding author upon request.

Conflicts of Interest

The authors declare that they have no conflicts of interest.

Acknowledgments

This research was supported by the Hebei Province Postdoctoral Research Project Merit-Based Funding Program (B2020005008).

References

- [1] X. Li, T. Li, and L. Peng, "Elastoplastic two-surface model for unsaturated cohesive soils under cyclic loading," *International Journal of Geomechanics*, vol. 20, no. 8, Article ID 04020122, 2020.
- [2] L. Zhu, G. Wang, F. Huang, Y. Li, W. Chen, and H. Hong, "Landslide susceptibility prediction using sparse feature extraction and machine learning models based on GIS and remote sensing," *IEEE Geoscience and Remote Sensing Letters*, vol. 15, pp. 1–5, 2021.
- [3] B. Bai, S. Jiang, L. Liu, X. Li, and H. Wu, "The transport of silica powders and lead ions under unsteady flow and variable injection concentrations," *Powder Technology*, vol. 387, pp. 22–30, 2021.
- [4] M. Aslani, J. Nazariafshar, and N. Ganjian, "Experimental study on shear strength of cohesive soils reinforced with stone columns," *Geotechnical and Geological Engineering*, vol. 37, no. 3, pp. 2165–2188, 2019.
- [5] A. M. Deganutti, P. R. Tecca, and R. Genevois, "The measure of friction angles for different types of granular material," *Journal of Mountain Science*, vol. 16, no. 4, pp. 769–777, 2019.
- [6] B. Bai, D. Rao, T. Chang, and Z. Guo, "A nonlinear attachment-detachment model with adsorption hysteresis for suspension-colloidal transport in porous media," *Journal of Hydrology*, vol. 578, Article ID 124080, 2019.
- [7] B. Bai, T. Xu, Q. Nie, and P. Li, "Temperature-driven migration of heavy metal Pb²⁺ along with moisture movement in unsaturated soils," *International Journal of Heat and Mass Transfer*, vol. 153, Article ID 119573, 2020.
- [8] M. Sánchez, A. Gens, M. V. Villar, and S. Olivella, "Fully coupled thermo-hydro-mechanical double-porosity formulation for unsaturated soils," *International Journal of Geomechanics*, vol. 16, no. 6, pp. 1–38, 2016.
- [9] E. Gholizadeh and M. Latifi, "A coupled hydro-mechanical constitutive model for unsaturated frictional and cohesive soil," *Computers and Geotechnics*, vol. 98, pp. 69–81, 2018.
- [10] B. Bai, D. Rao, T. Xu, and P. Chen, "SPH-FDM boundary for the analysis of thermal process in homogeneous media with a discontinuous interface," *International Journal of Heat and Mass Transfer*, vol. 117, pp. 517–526, 2018.
- [11] G. Yang and B. Bai, "Thermo-hydro-mechanical model for unsaturated clay soils based on granular solid hydrodynamics theory," *International Journal of Geomechanics*, vol. 19, no. 10, Article ID 04019115, 2019.
- [12] F. Huang, Z. Ye, S.-H. Jiang, J. Huang, Z. Chang, and J. Chen, "Uncertainty study of landslide susceptibility prediction considering the different attribute interval numbers of environmental factors and different data-based models," *Catena*, vol. 202, Article ID 105250, 2021.
- [13] F. Huang, Z. Cao, S.-H. Jiang, C. Zhou, J. Huang, and Z. Guo, "Landslide susceptibility prediction based on a semi-supervised multiple-layer perceptron model," *Landslides*, vol. 17, no. 12, pp. 2919–2930, 2020.
- [14] E. E. Alonso, A. Gens, and A. Josa, "A constitutive model for partially saturated soils," *Géotechnique*, vol. 40, no. 3, pp. 405–430, 1990.
- [15] B. Bai, L. Guo, and S. Han, "Pore pressure and consolidation of saturated silty clay induced by progressively heating/cooling," *Mechanics of Materials*, vol. 75, pp. 84–94, 2014.
- [16] S. L. Houston, "It is time to use unsaturated soil mechanics in routine geotechnical engineering practice," *Journal of Geotechnical and Geoenvironmental Engineering*, vol. 145, no. 5, Article ID 02519001, 2019.
- [17] B. Bai and Z. Su, "Thermal responses of saturated silty clay during repeated heating-cooling processes," *Transport in Porous Media*, vol. 93, no. 1, pp. 1–11, 2012.
- [18] B. Bai and X. Shi, "Experimental study on the consolidation of saturated silty clay subjected to cyclic thermal loading," *Geomechanics and Engineering*, vol. 12, no. 4, pp. 707–721, 2017.
- [19] K. S. Wong and D. Mašin, "Coupled hydro-mechanical model for partially saturated soils predicting small strain stiffness," *Computers and Geotechnics*, vol. 61, pp. 355–369, 2014.

- [20] B. Bai, F. Long, D. Rao, and T. Xu, "The effect of temperature on the seepage transport of suspended particles in a porous medium," *Hydrological Processes*, vol. 31, no. 2, pp. 382–393, 2017.
- [21] H. Ghasemzadeh and S. A. Ghoreishian Amiri, "A hydro-mechanical elastoplastic model for unsaturated soils under isotropic loading conditions," *Computers and Geotechnics*, vol. 51, pp. 91–100, 2013.
- [22] B. Bai, G.-C. Yang, T. Li, and G.-S. Yang, "A thermodynamic constitutive model with temperature effect based on particle rearrangement for geomaterials," *Mechanics of Materials*, vol. 139, Article ID 103180, 2019.
- [23] A. Hamrouni, D. Dias, and B. Sbartai, "Probability analysis of shallow circular tunnels in homogeneous soil using the surface response methodology optimized by a genetic algorithm," *Tunnelling and Underground Space Technology*, vol. 86, pp. 22–33, 2019.
- [24] Z. Zizka, B. Schoesser, M. Thewes, and T. Schanz, "Slurry shield tunneling: new methodology for simplified prediction of increased pore pressures resulting from slurry infiltration at the tunnel face under cyclic excavation processes," *International Journal of Civil Engineering*, vol. 17, no. 1, pp. 113–130, 2019.
- [25] L. Flessati and C. Di Prisco, "Deep tunnel faces in cohesive soils under undrained conditions: application of a new design approach," *European Journal of Environmental and Civil Engineering*, vol. 32, Article ID 1785332, 2018.
- [26] H. R. Huang, J. G. Zhu, and Z. R. Fang, "Triaxial test study of deformation and strength behavior of sand-gravel materials," *Water Resources and Power*, vol. 30, no. 7, pp. 87–89, 2012.
- [27] M. C. Liu, X. M. Huang, and Y. F. Gao, "Research on strength-deformation characteristics and nonlinear elastic model of rockfills," *Rock and Soil Mechanics*, vol. 25, no. 5, pp. 798–802, 2004.
- [28] G. Zhang and J. M. Zhang, "Study on behavior of coarse-grained soil and its modeling," *Rock and Soil Mechanics*, vol. 25, no. 10, pp. 1587–1591, 2004.
- [29] B. Indraratna, D. Ionescu, and H. D. Christie, "Shear behavior of railway ballast based on large-scale triaxial tests," *Journal of Geotechnical and Geoenvironmental Engineering*, vol. 124, no. 5, pp. 439–449, 1998.
- [30] P. Zhang, B. Bai, S. Jiang, P. Wang, and H. Li, "Transport and deposition of suspended particles in saturated porous media: effect of hydrodynamic forces and pore structure," *Water Science and Technology: Water Supply*, vol. 16, no. 4, pp. 951–960, 2016.
- [31] B. Bai, Q. Nie, Y. Zhang, X. Wang, and W. Hu, "Cotransport of heavy metals and SiO₂ particles at different temperatures by seepage," *Journal of Hydrology*, vol. 597, Article ID 125771, 2021.
- [32] D. Rao and B. Bai, "Study of the factors influencing diffusive tortuosity based on pore-scale SPH simulation of granular soil," *Transport in Porous Media*, vol. 132, no. 2, pp. 333–353, 2020.
- [33] W. Li, X. Fan, F. Huang et al., "Uncertainties analysis of collapse susceptibility prediction based on remote sensing and GIS: influences of different data-based models and connections between collapses and environmental factors," *Remote Sensing*, vol. 12, no. 24, p. 4134, 2020.
- [34] B. Mi and Y. Xiang, "Analysis of the limit support pressure of a shallow shield tunnel in sandy soil considering the influence of Seepage," *Symmetry*, vol. 12, no. 6, p. 1023, 2020.
- [35] S. Zingg and G. Anagnostou, "Tunnel face stability and the effectiveness of advance drainage measures in water-bearing ground of non-uniform permeability," *Rock Mechanics and Rock Engineering*, vol. 51, no. 1, 2017.
- [36] B. Bai, "Thermal response of saturated porous spherical body containing a cavity under several boundary conditions," *Journal of thermal Stresses*, vol. 36, no. 11, pp. 1217–1232, 2013.
- [37] B. Bai and T. Li, "Irreversible consolidation problem of a saturated porothermoelastic spherical body with a spherical cavity," *Applied Mathematical Modelling*, vol. 37, no. 4, pp. 1973–1982, 2013.
- [38] T. Qiu, C. Liu, X. Zhong, and Y. Zhu, "Experimental research on the impact of temperature on the adhesion characteristics of soil–structure interface," *Geofluids*, vol. 2020, Article ID 6675576, 9 pages, 2020.
- [39] Z.-G. Yan, Y. Zhang, Y. Shen, H.-H. Zhu, and Y. Lu, "A multilayer thermo-elastic damage model for the bending deflection of the tunnel lining segment exposed to high temperatures," *Tunnelling and Underground Space Technology*, vol. 95, Article ID 103142, 2020.
- [40] R. L. Kondner, "Hyperbolic stress-strain response: cohesive soils," *Journal of Soil Mechanics and Foundation Engineering*, vol. 89, no. 1, pp. 115–143, 1963.
- [41] J. M. Duncan and C.-Y. Chang, "Nonlinear analysis of stress and strain in soils," *Journal of Soil Mechanics and Foundation Engineering*, vol. 96, no. 5, pp. 1629–1653, 1970.
- [42] B. O. Hardin and V. P. Drnevich, "Shear modulus and damping in soils: design equations and curves," *Journal of the Soil Mechanics and Foundation Division*, vol. 98, no. 7, pp. 667–692, 1972.